



OPEN

Characterization of Vegard strain related to exceptionally fast Cu-chemical diffusion in $\text{Cu}_2\text{Mo}_6\text{S}_8$ by an advanced electrochemical strain microscopy method

Sebastian Badur¹, Diemo Renz², Marvin Cronau², Thomas Göddenhenrich¹, Dirk Dietzel^{1,3}, Bernhard Roling²✉ & André Schirmeisen^{1,3}✉

Electrochemical strain microscopy (ESM) has been developed with the aim of measuring Vegard strains in mixed ionic-electronic conductors (MIECs), such as electrode materials for Li-ion batteries, caused by local changes in the chemical composition. In this technique, a voltage-biased AFM tip is used in contact resonance mode. However, extracting quantitative strain information from ESM experiments is highly challenging due to the complexity of the signal generation process. In particular, electrostatic interactions between tip and sample contribute significantly to the measured ESM signals, and the separation of Vegard strain-induced signal contributions from electrostatically induced signal contributions is by no means a trivial task. Recently, we have published a compensation method for eliminating frequency-independent electrostatic contributions in ESM measurements. Here, we demonstrate the potential of this method for detecting Vegard strain in MIECs by choosing $\text{Cu}_2\text{Mo}_6\text{S}_8$ as a model-type MIEC with an exceptionally high Cu chemical diffusion coefficient. Even for this material, Vegard strains are only measurable around and above room-temperature and with proper elimination of electrostatics. The analysis of the measured Vegard strains gives strong indication that due to a high charge transfer resistance at the tip/interface, the local Cu concentration variations are much smaller than predicted by the local Nernst equation. This suggests that charge transfer resistances have to be analyzed in more detail in future ESM studies.

The growing efforts towards ecological sustainability put an ever increasing focus on the problem of energy storage, which is e.g. crucial to replace fossil fuels by renewable energies in the automotive sector. In this context, the optimization of electrochemical systems for energy storage does not only involve the application of materials with optimized chemical compositions¹, but recent analysis also has highlighted the potential impact of the materials nanostructures, with e.g. grain boundaries or interface regimes showing improved transport properties^{2–9}. Gaining nanoscale insight into the correlation between structure and electrochemical transport properties is thus not only a problem of fundamental interest^{10–12}, but it is also considered essential for further improvement of high-performance energy storage devices¹³. Consequently, the conventional approaches to measure macroscopic transport parameters need to be complemented by analyses at the nanoscale.

In order to monitor electrochemical processes with nanoscale resolution, a number of experimental techniques have been developed in recent years^{14–16}. In particular, atomic force microscopy (AFM) based methods are often used, since applying voltages to a conductive AFM tip allows to transfer classical concepts to the nanoscale, with the AFM tip acting as a nano-electrode. For example, in time-domain electrostatic force spectroscopy (TDESF), the time-dependent change of the electrostatic field strength between an oscillating AFM-tip and the sample after voltage-switching can be correlated to the ion dynamics in solid electrolytes^{17–20}. Alternatively, local

¹Institute of Applied Physics, Justus-Liebig-Universität Giessen, 35392 Giessen, Germany. ²Department of Chemistry, Philipps-Universität Marburg, Hans-Meerwein-Straße 4, 35032 Marburg, Germany. ³Center for Materials Research, Justus-Liebig-Universität Giessen, 35392 Giessen, Germany. ✉email: roling@staff.uni-marburg.de; andre.schirmeisen@ap.physik.uni-giessen.de

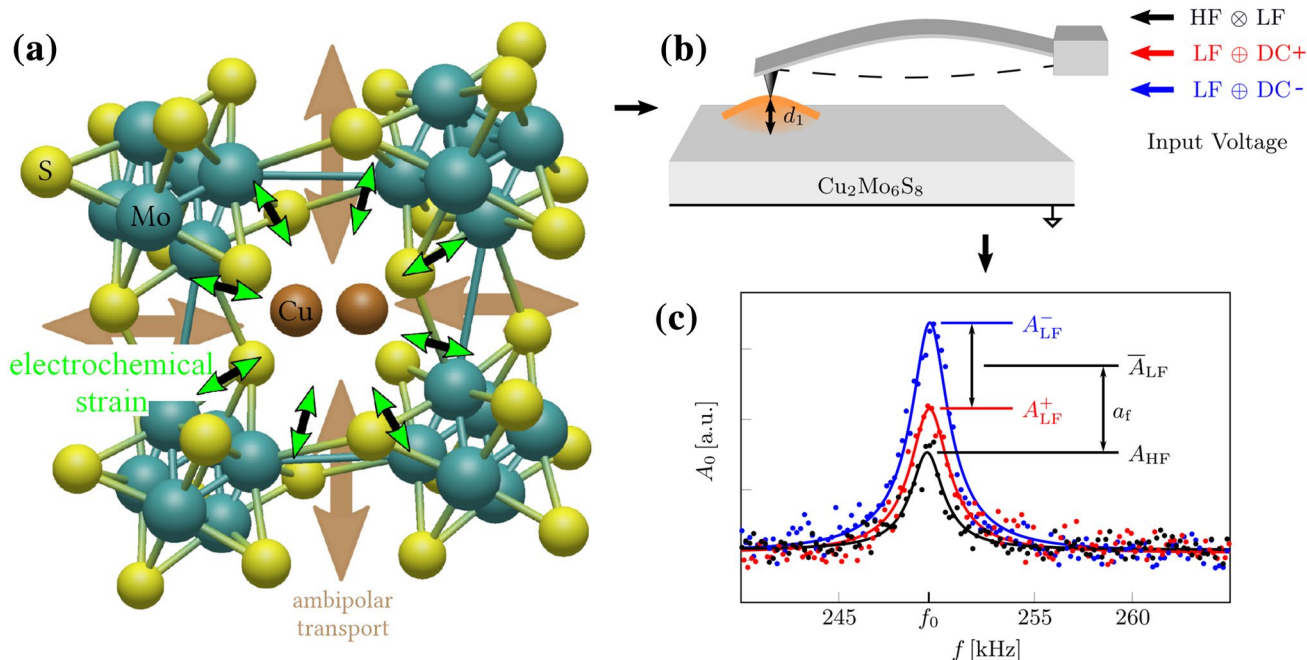


Figure 1. Scheme of material and setup. (a) Voltage driven ambipolar transport (indicated by larger brown arrows) on the Chevrel-phase $\text{Cu}_2\text{Mo}_6\text{S}_8$ induces Vegard-strain (indicated by small green arrows) due to change of Cu concentration (This subfigure was created using chemtool (1.6.14-4, <http://ruby.chemie.uni-freiburg.de/martin/chemtool/>) and inkscape (1.0.2-6, <https://inkscape.org>)). (b) The input voltages and the Vegard-strain d_1 drive the cantilever oscillation. As external voltages we applied an LF modulated high frequency voltage ($\text{HF} \otimes \text{LF}$), a low frequency excitation with positive DC voltage offset ($\text{LF} \oplus \text{DC}^+$), and a low frequency excitation with negative DC voltage offset ($\text{LF} \oplus \text{DC}^-$). (c) Exemplary resonance curves measured at 300K. A frequency related parameter a_f can then be extracted from the resonance oscillation amplitudes A_{LF}^+ , A_{LF}^- , and A_{HF} , that are resolved by band excitation and correspond to the different excitation voltages (see main text for details).

ionic transport properties can be correlated to the growth characteristics of metallic nanoparticles, that develop by redox reactions under application of cathodic overpotentials between tip and sample^{21–27}.

In the case of mixed ionic-electronic conductors (MIECs), acting as electrode materials in batteries, electrochemically induced changes in the chemical composition lead to Vegard strains, i.e. to the expansion or contraction of the material. For the local detection of such Vegard strains, the so-called electrochemical strain microscopy (ESM) technique has been developed^{28,29}. In this technique, an ac voltage bias applied to the tip at the contact resonance frequency leads to local chemical composition changes underneath the tip and thus to a local Vegard strain (see Fig. 1). The oscillating Vegard strain drives the contact resonance oscillation of the tip. Consequently, the method makes use of a contact-resonance amplification of the signal^{30–35}.

However, not only Vegard strains contribute to the measured ESM signals, but also electrostatic interactions between tip and sample^{13,36,37}. In several cases, the electrostatically induced ESM signals were considered to be even the dominant signals^{38,39}, and were, for instance, recently exploited for the analysis of local chemical distributions in solid state electrolytes⁴⁰.

Furthermore, it has been shown that also local contact mechanics at the tip/sample interface and the resulting dynamic lever shape during the contact resonance oscillation exert a strong influence on the measured signals^{36,41,42}.

Advanced methods for eliminating electrostatic effects are known from the closely related piezoresponse force microscopy (PFM): The so-called contact Kelvin Probe Force Microscopy (cKPFM) allows the quantitative measurement of electrostatic tip-sample interactions and its separation from electromechanical forces by continuous tracking of the local contact potential in combination with PFM measurements^{39,43–45}. Another recently introduced approach relies on the utilization of a laser Doppler vibrometer (LDV)^{38,46}. With this technique, non-local electrostatic signal contributions are effectively eliminated. Collins et al. showed that ESM hysteresis during voltage spectroscopy on ion conducting glasses, which is measured by conventional ESM/PFM setups and which had often been misunderstood as Vegard strain, can in fact be attributed to charge injection and electrostatic interactions³⁸. However, to our knowledge, none of these advanced techniques have been successfully applied to mixed conducting electrode materials in order to probe Vegard strains.

In order to eliminate the influence of electrostatics and contact mechanical signal contributions without losing resonance enhancement, we recently proposed a new compensation method based on band excitation, which exploits the distinct frequency dependences of Vegard strain and electrostatic contributions⁴⁷. In principle, this approach is similar to recent works^{33,48}, where Lock-in detection of the frequency-dependent ESM-signal in the low frequency range was discussed with respect to separation between Vegard strain and electrostatic interactions. In the case of the compensation method⁴⁷ however, only two frequencies are used, where information on

the Vegard strain is only contained in the low frequency signal, whereas the high-frequency signal is used as a reference to eliminate electrostatic contributions.

Here, we demonstrate the potential of this method for detecting Vegard strains in MIECs by choosing $\text{Cu}_2\text{Mo}_6\text{S}_8$ as a model-type MIEC material with an exceptionally high Cu chemical diffusion coefficient of $D_{\text{Cu}} = 3 \cdot 10^{-6} \text{ cm}^2/\text{s}$ at 300K (compare Fig. S1). Note that this value is about 5 to 6 orders of magnitude higher than the lithium diffusion coefficient in the common LIB electrode material LiCoO_2 ($D_{\text{Li}} \approx 10^{-11}$ to $10^{-12} \text{ cm}^2/\text{s}$)^{49–51}. Thus, it is expected that the Vegard strains in $\text{Cu}_2\text{Mo}_6\text{S}_8$ at typical contact resonance frequencies of several 100 kHz are considerably higher than those in typical LIB electrode materials.

$\text{Cu}_2\text{Mo}_6\text{S}_8$ belongs to the family of Chevrel phases with the general formula $\text{M}_x\text{Mo}_6\text{T}_8$ ($\text{M} = \text{metal}$, $\text{T} = \text{S}$, Se), which are especially known for their remarkable intercalation chemistry^{52–54}. Mo_6S_8 and Mo_6Se_8 do not only allow ultrafast and reversible insertion of monovalent cations like Li^+ or Na^+ but also of divalent cations like Cu^{2+} , Zn^{2+} or Mg^{2+} ^{54–56}. The Chevrel phase family contains various promising candidates for the development of high-performance rechargeable batteries, which might serve as an alternative to lithium ion batteries (LIBs)^{52,57–60}. Especially, $\text{Mg}_x\text{Mo}_6\text{S}_8$ -based systems are of great interest due to the high theoretical capacity and the great disposability of magnesium⁵⁸.

By applying the new compensation method⁴⁷ to $\text{Cu}_2\text{Mo}_6\text{S}_8$, we demonstrate that a proper elimination of electrostatic contributions is essential for quantitative measurements of Vegard strains. Even with such a proper elimination, Vegard strains can only be detected around and above room temperature. This finding is related to charge transfer resistances at the interfaces between tip and MIECs, which are anticipated to strongly influence the results of electromechanical AFM-experiments⁴⁸. In particular, our results give strong indication that a high charge transfer resistance at the tip/sample interface results in Cu concentration variations, which are much smaller than expected from the local Nernst equation.

Results and discussion

All ESM measurements were performed on $\text{Cu}_2\text{Mo}_6\text{S}_8$ using an atomic force microscope under ultrahigh vacuum conditions, where the sample temperature T was systematically varied between 200K and 400K (see “Materials and methods” for details). As shown in Fig. 1b, all electrical voltages were applied to the conductive diamond tip of the cantilever, with the counter electrode at the backside of the sample set to ground potential. If, for instance, a negative voltage is applied to the tip, Vegard strain can build up in a process where the movement of Cu^{2+} ions to the tip/sample-interface is coupled to the injection of electrons into the sample⁶¹.

The compensation method used in this work relies on applying different external voltages between the cantilever and the back-electrode of the sample. Detecting the peak values of the cantilever oscillations for each excitation basically allows to distinguish the different nanoscale contributions to the electromechanical response. More specifically, to quantify Vegard strain, three different excitations are applied. First, an amplitude modulated high frequency excitation is used as a reference, which exclusively contains signal contributions related to electrostatic forces acting on the cantilever since ambipolar diffusion is too slow to follow the high frequencies. In addition, also low frequency voltages with either positive or negative DC-bias are applied to the cantilever. In this case, surface displacements related to ambipolar diffusion can contribute to the signals, and as we will discuss later on, information about the Vegard strain can be gained from subtracting their average peak amplitudes from the reference amplitude, which yields the value a_f as shown in Fig. 1. In addition, this approach can also be applied to eliminate signal contributions related to local contact mechanics and topography-crosstalk. In this case the tip/sample contact needs to be described based on a Kelvin-Voigt model as detailed in⁴⁷.

Figure 1c further illustrates how the three different excitation voltages are used in our experiments: (i) low frequency excitation with positive DC voltage offset ($\text{LF} \oplus \text{DC}^+$), (ii) low frequency excitation with negative DC voltage offset ($\text{LF} \oplus \text{DC}^-$), and (iii) an LF modulated high frequency voltage ($\text{HF} \otimes \text{LF}$). For each of these excitations, the corresponding resonant oscillation amplitudes A_{LF}^+ , A_{LF}^- , and A_{HF} (Fig. 1c) were resolved by band excitation (BE)^{62,63} and recorded in addition to the topography signal of the AFM.

For estimating the magnitude of the Vegard strain, compositional variations induced by the voltage-biased tip have to be integrated over the diffusion length of the experiment. Therefore, the Vegard strain is expected to be proportional to the diffusion length L_D ³⁰,

$$d_1(f, T) \propto L_D = \sqrt{\frac{D(T)}{2\pi f}} \quad (1)$$

as long as L_D , which is dependent on both the temperature T and the excitation frequency f , is smaller than the tip diameter. At low frequencies ($f_{\text{LF}} \approx 250\text{kHz}$) and at high frequencies ($f_{\text{HF}} \approx 10\text{MHz}$), we obtain diffusion lengths of $L_D \approx 14\text{nm}$ and $L_D \approx 2\text{nm}$, respectively. Consequently, we expect significant contributions of Vegard strain to the ESM signal only at low frequencies, while the high-frequency measurements are dominated by electrostatic effects⁴⁷.

Based on these considerations, the Vegard strain at 250 kHz is given to a very good approximation by $d_1 \approx a_f = \bar{A}_{\text{LF}} - A_{\text{HF}}$, using the average LF amplitude $\bar{A}_{\text{LF}} = (A_{\text{LF}}^- + A_{\text{LF}}^+)/2$ and the reference amplitude A_{HF} , which is independent of both applied DC-voltages.

To illustrate the compensation method, Fig. 2 shows spatially resolved measurements of \bar{A}_{LF} , A_{HF} , and a_f in comparison with the topography. The ESM data was recorded for an ($0.8 \mu\text{m} \times 0.8 \mu\text{m}$) area, while voltages of $U_{\text{ac}} = 1\text{V}$ and $U_{\text{dc}} = \pm 1\text{V}$ were applied. All resonance amplitudes have been derived by band excitation covering a frequency range from 80kHz to 320kHz with 20 times averaging.

From Fig. 2 we can see that the signals related to the cantilever oscillations are highly dependent on location: (x, y) In these two regions, we find that both \bar{A}_{LF} and A_{HF} show high and low oscillation amplitudes, while the

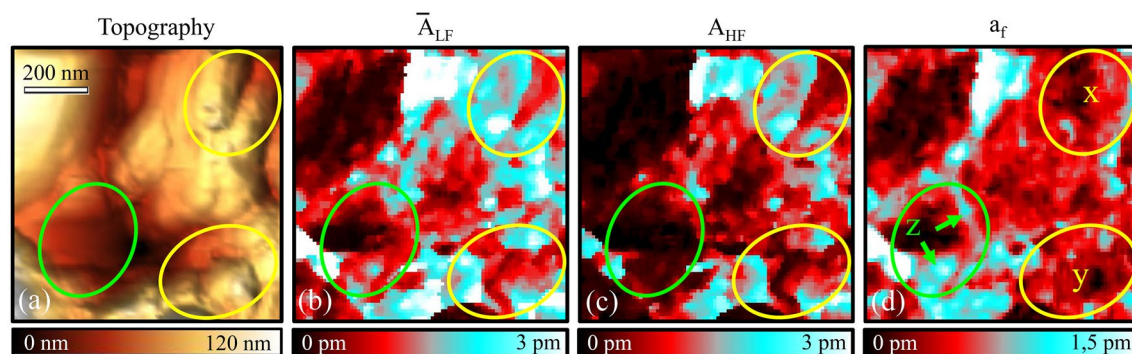


Figure 2. Electrochemical strain microscopy (ESM) on $\text{Cu}_2\text{Mo}_6\text{S}_8$ performed at room temperature with voltages of $U_{AC} = 1\text{V}$ and $U_{DC} = \pm 1\text{V}$. (a) Topography, (b) average low frequency response \bar{A}_{LF} , (c) high frequency response A_{HF} , and (d) the frequency related parameter a_f . Three regions have been marked to illustrate different strain related contrast (see main text for details).

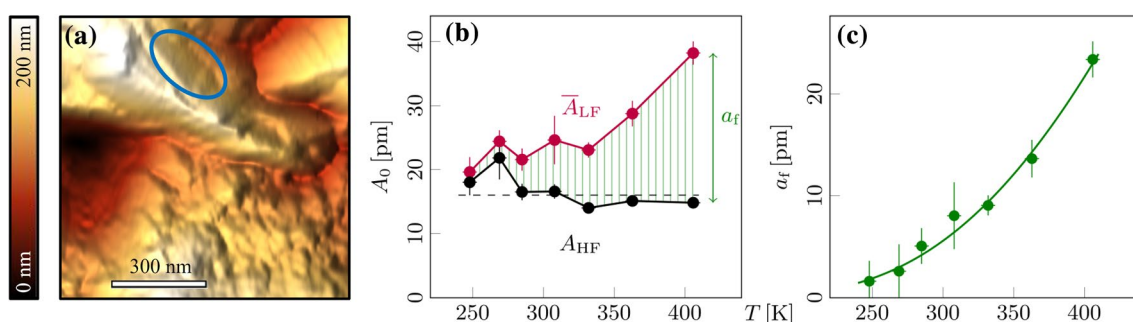


Figure 3. (a) Topography of the $\text{Cu}_2\text{Mo}_6\text{S}_8$ surface with an indication of the area under investigation in (b,c). (b) Linear plot of amplitudes A_{HF} (black) and \bar{A}_{LF} (red) averaged over the outlined region. The HF amplitude is constant over the temperature range, while the average LF amplitude increases with temperature. (c) The parameter a_f extracted from (b) increases exponentially with temperature.

corresponding signal amplitudes of a_f remain relatively constant around 0.5 pm. This suggests that unwanted signal contributions related to electrostatics and topographic effects dominate both \bar{A}_{LF} and A_{HF} , but are effectively eliminated in a_f , although both regions (x) and (y) show a certain roughness related to the very granular structure of the material. Thus we benefit from using a method that is less susceptible to mechanical cross-talk⁴⁷. Finally, it is known that ambipolar diffusion depends on crystallographic orientation and grain size and can be favored at defects such as grain boundaries^{64,65}. Such effects appear to be evident in region (z), where large values of \bar{A}_{LF} and a_f , but not of A_{HF} , are observed, suggesting large contributions of Vegard strain to the low-frequency signals.

As a next step, we performed temperature-dependent ESM measurements in a range from 250K up to 400K on a homogeneous area on top of a single large grain, as indicated by the outline in Fig. 3. For a clear detection of signals also at low temperatures, we used $U_{ac} = 2.5\text{V}$ and $U_{dc} = \pm 2.5\text{V}$. We find that the average values of \bar{A}_{LF} within the marked area are increasing with temperature, while A_{HF} remains almost constant with an amplitude of about 16pm (Fig. 3b). The small temperature dependence of A_{HF} supports our argument given above that the A_{HF} signal is governed by electrostatic interactions. For technical reasons (see “Materials and Methods” section), slight variations in A_{HF} may result from differences in sensitivity and normal force. However, since both A_{HF} and \bar{A}_{LF} are equally affected by this, the effects largely cancel out when calculating a_f . Ultimately, a_f increases strongly with increasing temperature and exhibits values ranging from roughly 2pm at 250K up to 25pm at 400K (Fig. 3c).

According to Eq. 1, the temperature dependence of the Vegard strain a_f should be influenced by the temperature dependence of the chemical diffusion coefficient $D(T)$. Macroscopic measurements of $D(T)$ by means of impedance spectroscopy yield an Arrhenius-type temperature dependence $D(T) \propto e^{-E_A/RT}$ with an activation energy $E_{\text{macro}} = 23.0 \pm 1.0 \frac{\text{kJ}}{\text{mol}}$, (see Fig. S1 and related information in the Supporting Information). If the temperature dependence of the Vegard strain a_f was exclusively due to temperature dependence of the chemical diffusion coefficient, the activation energy in the ESM experiments would be given by:

$$E_A = -2R \frac{\partial \ln a_f(T)}{\partial (1/T)} \quad (2)$$

In Fig. 4, we show an Arrhenius plot of $a_f(T)$ (green symbols) yielding an activation energy of $E_A = 27.1 \pm 1.6 \frac{\text{kJ}}{\text{mol}}$, which is close to the macroscopic value for $D(T)$. We added also the data for the low-frequency signal \bar{A}_{LF} (red data points) to Fig. 4. The weak temperature dependence of \bar{A}_{LF} as compared to $a_f(T)$, as already evident in

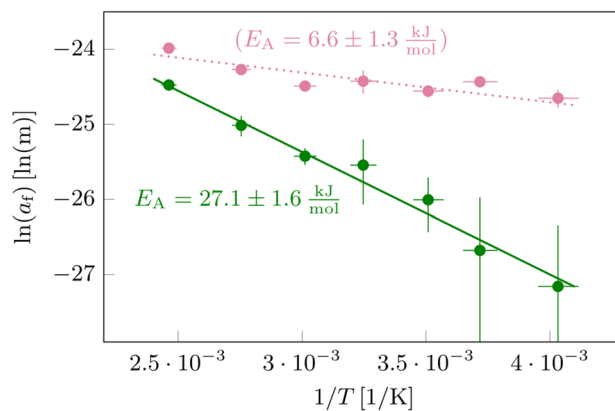


Figure 4. Arrhenius Plots of the ESM data recorded for a single grain (see Fig. 3): (Green) Frequency-dependent Vegard strain parameter a_f plotted vs. the inverse temperature. (Red) Average LF amplitude \bar{A}_{LF} plotted vs. the inverse temperature. In both cases, the slope represents an activation energy barrier E_A for ambipolar diffusion with quantitative values as indicated in the figure. Please note that the temperature-dependent analysis of \bar{A}_{LF} does not result in a meaningful energy barrier for ambipolar diffusion, but was rather added to highlight the problems, that can arise from temperature independent contributions, which significantly reduce the slope.

Fig. 3, points to the significant contribution of electrostatics to the \bar{A}_{LF} and emphasizes the importance of the compensation method.

Next we analyze the results obtained for the Vegard strains $d_1 \approx a_f$ in relation to theoretical predictions. In Balke et al.⁶⁶, the following relation between the Vegard strain d_1 and the applied ac voltage U_{ac} is given:

$$d_1 = 2(1 + \nu) \beta \frac{U_{ac}}{\eta} \sqrt{\frac{D(T)}{2\pi f}} \quad (3)$$

Here, ν and β denote Poisson's ratio and the Vegard coefficient, respectively. The Vegard coefficient relates the relative expansion or contraction of the crystal lattice to the relative variation in the Cu concentration. The quantity $\eta = U_{ac} \cdot c_{Cu} / \Delta c_{Cu}$ relates the applied ac voltage to the periodic relative variation in the Cu concentration at the tip/sample interface. Consequently, the relative Cu concentration variation can be written as:

$$\frac{\Delta c_{Cu}}{c_{Cu}} = \frac{d_1}{2(1 + \nu) \beta \sqrt{\frac{D(T)}{2\pi f}}} \quad (4)$$

Thus, Eq. (3) and the eq. for η imply that U_{ac} leads to a periodic variation of $\Delta c_{Cu}/c_{Cu}$ and, in turn, to a periodic variation of the Vegard strain. Typical values for Poisson's ratio are around 0.25. In order to estimate the Vegard coefficient β , we average over all crystal orientations of the hexagonal $\text{Cu}_2\text{Mo}_6\text{S}_8$ lattice by considering the total volume of the crystal lattice V as a function of the Cu content x . This approach is required since the radial chemical diffusion below the AFM-tip always leads to a geometrical averaging effect, even in a single measurement.

From x-ray diffraction data in Ref.⁶⁷, the estimated Vegard coefficient around $x = 2$ is $\beta \approx \frac{1}{3} \frac{d \ln V}{d \ln x} = 0.03$. With $D_{Cu}(300\text{ K}) = 3 \cdot 10^{-6} \text{ cm}^2/\text{s}$, $\omega \approx 2\pi \cdot 250\text{ kHz}$ and $d_1(300\text{ K}) \approx a_f(300\text{ K}) = 5 \text{ pm}$, we find that $\frac{\Delta c_{Cu}}{c_{Cu}}(300\text{ K}) = \frac{\Delta x_{Cu}}{x_{Cu}}(300\text{ K}) \approx 0.005$.

From the galvanostatic titration curves shown in Ref.⁶⁷, it is evident that such tiny concentration changes correspond to only a few mV changes in the thermodynamic reduction potential of $\text{Cu}_2\text{Mo}_6\text{S}_8$. Considering the applied ac voltage $U_{ac} = 2.5\text{ V}$, this implies that there must be a huge resistance R_{CT} (and thus overpotential) for electronic charge transfer at the tip/sample interface. In the ESI Part B, the overall resistance $R_{total} = R_{CT} + R_D$, with R_D denoting the spreading diffusion resistance of the probed subvolume, was estimated based on the assumption that the measured Vegard strain depends essentially on the charge flow and that orientation-dependent strain effects are of second order. As shown in the online supporting material (Part B), R_{total} is around $5 \cdot 10^{10} \Omega$. For comparison, the spreading diffusion resistance of the probed subvolume below the tip was estimated to be around $3 \cdot 10^5 \Omega$. i.e. about five orders of magnitude lower than R_{CT} (see Supporting Material, Part B). This implies that $R_{CT} \approx R_{total} \approx 5 \cdot 10^{10} \Omega$. While the absolute charge transfer resistance is high, the area-normalized value $10^{-1} \Omega \text{ cm}^2$ is comparably low (nominal AFM tip radius of about 10 nm). These estimations confirm that the charge flow and Vegard strain are limited by interfacial charge transfer rather than chemical diffusion in the probed subvolume, which is in contrast to the assumption made in former ESM studies that charge transfer resistances were small or even negligible^{66,68}, but are in line with a recent analysis of charge transfer resistances in AFM experiments⁴⁸. Thus, in future ESM measurements, more attention has to be paid to contact or charge transfer resistances at the tip/sample interface. If these resistances can be reduced, e.g. by using suitable tips and/or by removing possible resistive layers at the sample surface, larger ESM signals at lower ac voltages should be detectable.

Conclusion

A recently introduced compensation method for the separation of electrostatic and electromechanical signal (e.g. Vegard strain) contributions in electrochemical strain microscopy (ESM) has been applied to the mixed ion/electron conductor (MIEC) $\text{Cu}_2\text{Mo}_6\text{S}_8$, a model-type material with an extraordinary high copper diffusion coefficient of $D_{\text{Cu}} = 3 \cdot 10^{-6} \text{ cm}^2/\text{s}$. To our knowledge, this work presents the first temperature-dependent Vegard strain measurements by an advanced ESM method. The potential of the new method was demonstrated by temperature-dependent measurements on a single grain, clearly achieving a successful separation of a temperature-independent electrostatic contribution and a thermally activated Vegard strain. We found that even for this material, the contributions of Vegard strain and of electrostatics to the overall ESM signal are in the same range at room temperature. Thus, elimination of electrostatic contributions is crucial for detecting and analyzing Vegard strain contributions. Our results give strong indication that in the case of $\text{Cu}_2\text{Mo}_6\text{S}_8$, the Vegard strain is limited by a large charge transfer resistance at the tip/sample interface and not by chemical diffusion in the probed subvolume of the sample. Thus, in future ESM measurements, more attention should be paid to contact/charge transfer resistances at the tip/sample interface.

Methods

All temperature-dependent AFM measurements have been performed under ultra-high vacuum conditions using a variable temperature atomic force microscope (VT-AFM) by ScientaOmicron. The temperature-dependent experiments have been performed as a series of spatially resolved ESM measurements at fixed temperatures between 200K up to 400K. During temperature changes, we have carefully monitored and tracked the sample position to eliminate drift effects. Thereby, the exact same area of the sample was analyzed at each temperature.

The AFM was operated in contact mode using a normal force setpoint of 10nN. After each temperature change, the laser spot position on the cantilever was readjusted, a procedure with potentially minor influence on the normal force. Throughout the experiments we used commercial cantilevers with a conductive and non-abrasive single crystal diamond tip (Adama Innovations, AD-E-0.5-AS). These cantilevers are characterized by a nominal tip radius of $R \lesssim 10 \text{ nm}$, a spring constant of 0.5N/m, and a free resonance frequency of 30kHz.

Received: 10 May 2021; Accepted: 4 August 2021

Published online: 13 September 2021

References

- Lu, Y., Zhang, Q. & Chen, J. Recent progress on lithium-ion batteries with high electrochemical performance. *Sci. China Chem.* **62**, 533–548 (2019).
- Sata, N., Eberman, K., Eberl, K. & Maier, J. Mesoscopic fast ion conduction in nanometre-scale planar heterostructures. *Nature* **408**, 946–949. <https://doi.org/10.1038/35050047> (2000).
- Sata, N. Enhanced ionic conductivity and mesoscopic size effects in heterostructures of BaF_2 and CaF_2 . *Solid State Ionics* **154–155**, 497–502. [https://doi.org/10.1016/S0167-2738\(02\)00488-5](https://doi.org/10.1016/S0167-2738(02)00488-5) (2002).
- Zhu, J., Lu, L. & Zeng, K. Nanoscale mapping of lithium-ion diffusion in a cathode within an all-solid-state lithium-ion battery by advanced scanning probe microscopy techniques. *ACS Nano* **7**, 1666–1675. <https://doi.org/10.1021/nn305648j> (2013).
- Indris, S., Heitjans, P., Roman, H. E. & Bunde, A. Nanocrystalline versus microcrystalline $\text{Li}_2\text{O}:\text{B}_2\text{O}_3$ composites: anomalous ionic conductivities and percolation theory. *Phys. Rev. Lett.* **84**, 2889–2892 (2000).
- Schirmeisen, A. *et al.* Fast interfacial ionic conduction in nanostructured glass ceramics. *Phys. Rev. Lett.* **98**, 225901. <https://doi.org/10.1103/PhysRevLett.98.225901> (2007).
- Yang, S., Yan, B., Lu, L. & Zeng, K. Grain boundary effects on Li-ion diffusion in a $\text{Li}_{1.2}\text{Co}_{0.13}\text{Ni}_{0.13}\text{Mn}_{0.54}\text{O}_2$ thin film cathode studied by scanning probe microscopy techniques. *RSC Adv.* **6**, 94000–94009. <https://doi.org/10.1039/C6RA17681J> (2016).
- Xia, H. & Lu, L. Texture effect on the electrochemical properties of LiCoO_2 thin films prepared by PLD. *Electrochim. Acta* **52**, 7014–7021. <https://doi.org/10.1016/j.electacta.2007.05.019> (2007).
- Fabbri, E., Pergolesi, D. & Traversa, E. Ionic conductivity in oxide heterostructures: the role of interfaces. *Sci. Technol. Adv. Mater.* **11**, 054503. <https://doi.org/10.1088/1468-6996/11/5/054503> (2010).
- Zhang, B. *et al.* Mechanisms and properties of ion-transport in inorganic solid electrolytes. *Energy Storage Mater.* **10**, 139–159 (2018).
- Sata, N., Jin-Phillipp, N., Eberl, K. & Maier, J. Enhanced ionic conductivity and mesoscopic size effects in heterostructures of BaF_2 and CaF_2 . *Solid State Ionics* **154**, 497–502 (2002).
- Indris, S., Heitjans, P., Roman, H. E. & Bunde, A. Nanocrystalline versus microcrystalline $\text{Li}_2\text{O}:\text{B}_2\text{O}_3$ composites: anomalous ionic conductivities and percolation theory. *Phys. Rev. Lett.* **84**, 2889 (2000).
- Kalinin, S. V. *et al.* toward electrochemical studies on the nanometer and atomic scales: progress, challenges, and opportunities. *ACS Nano* **13**, 9735–9780 (2019).
- Wang, Z., Kotobuki, M., Lu, L. & Zeng, K. Nanoscale characterization of solid electrolyte by Scanning Probe Microscopy techniques. *Electrochim. Acta* **334**, 135553 (2020).
- Kalinin, S. *et al.* Li-ion dynamics and reactivity on the nanoscale. *Mater. Today* **14**, 548–558 (2011).
- Bentley, C. L. *et al.* Nanoscale electrochemical mapping. *Anal. Chem.* **91**, 84–108 (2018).
- Schirmeisen, A. & Roling, B. Characterizing ion dynamics in nanoscopic volumes: time-domain electrostatic force spectroscopy on solid electrolytes. *Monatshefte für Chemie-Chem. Monthly* **140**, 1103–1112 (2009).
- Taskiran, A., Schirmeisen, A., Fuchs, H., Bracht, H. & Roling, B. Time-domain electrostatic force spectroscopy on nanostructured lithium-ion conducting glass ceramics: analysis and interpretation of relaxation times. *Phys. Chem. Chem. Phys.* **11**, 5499–5505 (2009).
- Schirmeisen, A. *et al.* Fast interfacial ionic conduction in nanostructured glass ceramics. *Phys. Rev. Lett.* **98**, 225901 (2007).
- Schirmeisen, A. *et al.* Probing ion transport at the nanoscale: time-domain electrostatic force spectroscopy on glassy electrolytes. *Appl. Phys. Lett.* **85**, 2053–2055 (2004).
- Kruempelmann, J. *et al.* AFM tip-induced metal particle formation on laser-structured and on unstructured surfaces of solid-state ion conductors. *Solid State Ionics* **234**, 46–50 (2013).
- Arruda, T. M., Kumar, A., Kalinin, S. V. & Jesse, S. The partially reversible formation of Li-metal particles on a solid Li electrolyte: applications toward nanobatteries. *Nanotechnology* **23**, 325402 (2012).

23. Arruda, T. M., Kumar, A., Kalinin, S. V. & Jesse, S. Mapping irreversible electrochemical processes on the nanoscale: ionic phenomena in Li ion conductive glass ceramics. *Nano Lett.* **11**, 4161–4167. <https://doi.org/10.1021/nl202039v> (2011).
24. Krümpelmann, J. *et al.* Nanoscale electrochemical measurements on a lithium-ion conducting glass ceramic: in-situ monitoring of the lithium particle growth. *Electrochem. Commun.* **18**, 74–77. <https://doi.org/10.1016/j.elecom.2012.02.019> (2012).
25. Kumar, A. *et al.* Nanometer-scale mapping of irreversible electrochemical nucleation processes on solid Li-ion electrolytes. *Sci. Rep.* **3**, 1621. <https://doi.org/10.1038/srep01621> (2013).
26. Kumar, A. *et al.* Frequency spectroscopy of irreversible electrochemical nucleation kinetics on the nanoscale. *Nanoscale* **5**, 11964–11970. <https://doi.org/10.1039/C3NR03953F> (2013).
27. Lushta, V., Dietzel, D., Roling, B. & Schirmeisen, A. Nanoscale characterization of ion mobility by temperature-controlled nanoparticle growth. *ACS Appl. Mater. Interfaces* **11**, 5476–5483 (2019).
28. Balke, N. *et al.* Decoupling electrochemical reaction and diffusion processes in ionically-conductive solids on the nanometer scale. *ACS Nano* **4**, 7349–7357 (2010).
29. Kalinin, S. V. *et al.* ESM of ionic and electrochemical phenomena on the nanoscale. *Adv. Mater. Process.* **169**, (2011).
30. Morozovska, A. N., Eliseev, E. A., Balke, N. & Kalinin, S. V. Local probing of ionic diffusion by electrochemical strain microscopy: spatial resolution and signal formation mechanisms. *J. Appl. Phys. Vol. 108, Issue 5, pp. 053712-053712-21* (2010). **108**, 053712. <https://doi.org/10.1063/1.3460637>.
31. Li, J., Li, J.-F., Yu, Q., Chen, Q. N. & Xie, S. Strain-based scanning probe microscopies for functional materials, biological structures, and electrochemical systems. *J. Materiomics* **1**, 3–21 (2015).
32. Balke, N. *et al.* Quantification of surface displacements and electromechanical phenomena via dynamic atomic force microscopy. *Nanotechnology* **27**, 425707 (2016).
33. Alikin, D. O. *et al.* Quantitative characterization of the ionic mobility and concentration in Li-battery cathodes via low frequency electrochemical strain microscopy. *Nanoscale* (2018).
34. Schön, N. *et al.* Correlative electrochemical strain and scanning electron microscopy for local characterization of the solid state electrolyte $\text{Li}_{1.3}\text{Al}_{0.3}\text{Ti}_{1.7}(\text{PO}_4)_3$. *Beilstein. J. Nanotechnol.* **9**, 1564–1572 (2018).
35. Simolka, M., Heim, C., Friedrich, K. & Hiesgen, R. Visualization of local ionic concentration and diffusion constants using a tailored electrochemical strain microscopy method. *J. Electrochem. Soc.* **166**, A5496–A5502 (2019).
36. Lushta, V., Bradler, S., Roling, B. & Schirmeisen, A. Correlation between drive amplitude and resonance frequency in electrochemical strain microscopy: influence of electrostatic forces. *J. Appl. Phys.* **121**, 224302 (2017).
37. Balke, N. *et al.* Quantification of in-contact probe-sample electrostatic forces with dynamic atomic force microscopy. *Nanotechnology* **28**, 065704 (2017).
38. Collins, L., Liu, Y., Ovchinnikova, O. S. & Proksch, R. Quantitative electromechanical atomic force microscopy. *ACS Nano* **13**, 8055–8066 (2019).
39. Vasudevan, R. K., Balke, N., Maksymovych, P., Jesse, S., Kalinin, S. V. Ferroelectric or non-ferroelectric: why so many materials exhibit “ferroelectricity” on the nanoscale. *Appl. Phys. Rev.* **4**, 021302 (2017).
40. Schön, N. *et al.* Signal origin of electrochemical strain microscopy and link to local chemical distribution in solid state electrolytes. *Small Methods* **5**, 2001279. <https://doi.org/10.1002/smt.202001279> (2021).
41. Bradler, S., Schirmeisen, A. & Roling, B. Amplitude quantification in contact-resonance-based voltage-modulated force spectroscopy. *J. Appl. Phys.* **122**, 065106 (2017).
42. Yang, S. M. *et al.* Decoupling indirect topographic cross-talk in band excitation piezoresponse force microscopy imaging and spectroscopy. *Appl. Phys. Lett., Volume 108, Issue 25, id.252902* **108**, 252902. <https://doi.org/10.1063/1.4954276> (2016).
43. Ziatdinov, M. *et al.* Super-resolution and signal separation in contact Kelvin probe force microscopy of electrochemically active ferroelectric materials. *J. Appl. Phys.* **128**, 055101. <https://doi.org/10.1063/5.0013847> (2020).
44. Balke, N. *et al.* Exploring local electrostatic effects with scanning probe microscopy: implications for piezoresponse force microscopy and triboelectricity. *ACS Nano* **8**, 10229–10236. <https://doi.org/10.1021/nn505176a> (2014).
45. Yang, S. M. *et al.* Mixed electrochemical-ferroelectric states in nanoscale ferroelectrics. *Nat. Phys.* **13**, 8 (2017).
46. Labuda, A. & Proksch, R. Quantitative measurements of electromechanical response with a combined optical beam and interferometric atomic force microscope. *Appl. Phys. Lett.* **5**, (2015).
47. Badur, S. *et al.* Voltage- and frequency-based separation of nanoscale electromechanical and electrostatic forces in contact resonance force microscopy: implications for the analysis of battery materials. *ACS Appl. Nano Mater.* (2020).
48. Romanyuk, K. *et al.* Local electronic transport across probe/ionic conductor interface in scanning probe microscopy. *Ultramicroscopy* **220**, 113147. <https://doi.org/10.1016/j.ultramic.2020.113147> (2021).
49. Xie, J. *et al.* Orientation dependence of Li-ion diffusion kinetics in LiCoO_2 thin films prepared by RF magnetron sputtering. *Solid State Ionics* **179**, 362–370. <https://doi.org/10.1016/j.ssi.2008.02.051> (2008).
50. Tang, S. B., Lai, M. O. & Lu, L. Li-ion diffusion in highly (0 0 3) oriented LiCoO_2 thin film cathode prepared by pulsed laser deposition. *J. Alloys Compd.* **4**, (2008).
51. Rho, Y. H. & Kanamura, K. Li^+ -ion diffusion in LiCoO_2 thin film prepared by the poly(vinylpyrrolidone) sol-gel method. *J. Electrochem. Soc.* **151**, A1406. <https://doi.org/10.1149/1.1779333> (2004).
52. Barbosa, J. *et al.* In situ synchrotron powder diffraction study of Cd intercalation into Chevrel phases: crystal structure and kinetic effect. *Inorg. Chem.* **58**, 2158–2168. <https://doi.org/10.1021/acs.inorgchem.8b03259> (2019).
53. Levi, E., Mitelman, A., Aurbach, D. & Brunelli, M. Structural mechanism of the phase transitions in the Mg–Cu– Mo_6S_8 system probed by ex situ synchrotron x-ray diffraction. *Chem. Mater.* **19**, 5131–5142. <https://doi.org/10.1021/cm0715489> (2007).
54. Levi, E., Gershinsky, G., Aurbach, D. & Isnard, O. Crystallography of Chevrel phases, MMo_6T_8 (M = Cd, Na, Mn, and Zn, T = S, Se) and their cation mobility. *Inorg. Chem.* **48**, 8751–8758. <https://doi.org/10.1021/ic900805g> (2009).
55. Levi, E., Gershinsky, G., Aurbach, D., Isnard, O. & Ceder, G. New insight on the unusually high ionic mobility in Chevrel phases. *Chem. Mater.* **21**, 1390–1399. <https://doi.org/10.1021/cm900033v> (2009).
56. Levi, M. *et al.* Phase transitions and diffusion kinetics during Mg^{2+} - and Li^+ -ion insertions into the Mo_6S_8 chevrel phase compound studied by PITT. *Electrochim. Acta* **49**, 3201–3209. <https://doi.org/10.1016/j.electacta.2004.02.034> (2004).
57. Mei, L. *et al.* Chevrel phase Mo_6T_8 (T = S, Se) as electrodes for advanced energy storage. *Small* **13**, 1701441. <https://doi.org/10.1002/sml.201701441> (2017).
58. Levi, E., Levi, M.D., Chasid, O. & Aurbach, D. A review on the problems of the solid state ions diffusion in cathodes for rechargeable Mg batteries. *J. Electroceram.* **7** (2009).
59. Aurbach, D. *et al.* ChemInform abstract: prototype systems for rechargeable magnesium batteries. *ChemInform* **32**. <https://doi.org/10.1002/chin.200103014> (2001).
60. Lee, B., No, W. J. & Oh, S. H. Unravelling the role of interfacial chemistry evolution in the kinetics of zinc insertion into chevrel phase. *J. Power Sources* **478**, 229086. <https://doi.org/10.1016/j.jpowsour.2020.229086> (2020).
61. Renz, D., Cronau, M. & Roling, B. Determination of lithium diffusion coefficients in single battery active material particles by using an AFM-based steady-state diffusion depolarization technique. *J. Phys. Chem. C* **125**, 2230–2239. <https://doi.org/10.1021/acs.jpcc.0c07751> (2021).
62. Jesse, S. & Kalinin, S. V. Band excitation in scanning probe microscopy: sines of change. *J. Phys. D Appl. Phys.* **44**, 464006 (2011).
63. Jesse, S., Kalinin, S. V., Proksch, R., Baddorf, A. P. & Rodriguez, B. J. The band excitation method in scanning probe microscopy for rapid mapping of energy dissipation on the nanoscale. *Nanotechnology* **18**, 435503 (2007).

64. Yamakawa, S., Yamasaki, H., Koyama, T. & Asahi, R. Numerical study of Li diffusion in polycrystalline LiCoO₂. *J. Power Sources* **223**, 199–205 (2013).
65. Eshghinejad, A., Esfahani, E. N., Lei, C. & Li, J. Resolving local electrochemistry at the nanoscale via electrochemical strain microscopy: Modeling and experiments. arXiv preprint [arXiv:1704.01158](https://arxiv.org/abs/1704.01158) (2017).
66. Balke, N. *et al.* Nanoscale mapping of ion diffusion in a lithium-ion battery cathode. *Nat. Nanotechnol.* **5**, 749–754. <https://doi.org/10.1038/nnano.2010.174> (2010).
67. Fischer, C., Gocke, E., Stege, U. & Schoellhorn, R. Molybdenum cluster chalcogenides: in situ x-ray studies on the formation of cuxmo6s8 via electron/ion transfer. *J. Solid State Chem.* **102**, 54–68. <https://doi.org/10.1006/jssc.1993.1007> (1993).
68. Chung, D.-W., Balke, N., Kalinin, S. V. & Garcia, R. E. Virtual electrochemical strain microscopy of polycrystalline LiCoO₂ films. *J. Electrochem. Soc.* **158**, A1083. <https://doi.org/10.1149/1.3619775> (2011).

Acknowledgements

DD, BR, and AS acknowledge support by the German Research Foundation (Projects Di917/7-1, Ro1213/14-1, Schi619/14-1).

Author contributions

S.B., T.G., D.R., D.D, B.R., and A.S. conceived the experiments; S.B., T.G., D.R., M.C., and D.D. conducted the experiments and analyzed the results; All authors reviewed the manuscript.

Funding

Open Access funding enabled and organized by Projekt DEAL.

Competing interests

The authors declare no competing interests.

Additional information

Supplementary Information The online version contains supplementary material available at <https://doi.org/10.1038/s41598-021-96602-2>.

Correspondence and requests for materials should be addressed to B.R. or A.S.

Reprints and permissions information is available at www.nature.com/reprints.

Publisher's note Springer Nature remains neutral with regard to jurisdictional claims in published maps and institutional affiliations.



Open Access This article is licensed under a Creative Commons Attribution 4.0 International License, which permits use, sharing, adaptation, distribution and reproduction in any medium or format, as long as you give appropriate credit to the original author(s) and the source, provide a link to the Creative Commons licence, and indicate if changes were made. The images or other third party material in this article are included in the article's Creative Commons licence, unless indicated otherwise in a credit line to the material. If material is not included in the article's Creative Commons licence and your intended use is not permitted by statutory regulation or exceeds the permitted use, you will need to obtain permission directly from the copyright holder. To view a copy of this licence, visit <http://creativecommons.org/licenses/by/4.0/>.

© The Author(s) 2021